ELSEVIER

Thermochimica Acta 330 (1999) 21–38

thermochimica acta

Temperature-modulated differential scanning calorimetry of reversible and irreversible first-order transitions[1,2]

B. Wunderlich*, A. Boller, I. Okazaki, K. Ishikiriyama, W. Chen, M. Pyda, J. Pak, I. Moon, R. Androsch

Department of Chemistry, The University of Tennessee, Knoxville, TN 37996-1600, USA
The Chemical and Analytical Sciences Division, Oak Ridge National Laboratory, Oak Ridge, TN 37831-6197, USA

Received 12 August 1998; accepted 27 November 1998

Abstract

Temperature-modulated differential scanning calorimetry of first-order transitions has led to many new observations. Some of these involve non-linear processes or deal with transformations of practically instantaneous response. The latter may cause serious lags within the calorimeter due to limited thermal conductivity of the sample and the instrument. In both cases the ''reversing heat capacity'' or a ''complex heat capacity'' is not a precise representation of the transition since both are computed from abbreviated Fourier transforms, limited to the evaluation of the first harmonic component. One has in these cases to work in the time-domain with the raw output. But even from these analyses in the time-domain many interesting new insights about the transition and the calorimeter performance can be generated.

Keywords: Temperature-modulated calorimetry; Heat capacity; First-order transition; Lissajous figures; Indium; Paraffin; Liquid crystal; Polymer

1. Introduction

Temperature-modulated differential scanning calorimetry (TMDSC) [1–3] has become a well-established new technique of measurement. Its development can be followed by the discussions held during the last three Lähnwitz seminars (nos. 3–5). Our lecture contributed to the third seminar dealt with ''Modulated DSC – Capabilities and Limits.'' In this lecture we derived the mathematical description of the data treatment and established the run parameters for the quasi-isothermal method of measurement. Much of the content of the lecture was published in references [4,5]. The fourth seminar was published in a collected volume of *Thermochimica Acta* [6]. Our contribution consisted of the ''Specific-Heat Capacity Determination by Modulated DSC and its Separation from Transition Effects'' [7]. Besides methods of heat-capacity measurement and calculation, the main tran-

*Corresponding author. Tel.: +1-423-974-0652; fax: +1-423-974-3419.

[1]Presented at the Fifth Lähnwitz Seminar.

[2]The submitted manuscript has been authored by a contractor of the US Government under the contract no. DE-AC05-96OR22464. Accordingly, the US Government retains a non-exclusive, royalty-free license to publish, or reproduce the published form of this contribution, or allow others to do so, for US Government purposes.

0040-6031/99/$ – see front matter
PII: S0040-6031(99)00037-4

sition discussed was the glass transition. Even without an enthalpy of transition, clear deviations from linearity were observed for the apparent heat capacity in the glass transition region and could be linked quantitatively to the kinetics of the process [8–11]. Also, at the fourth Lähnwitz seminar a new observation was reported: quasi-isothermal TMDSC revealed a small, reversing contribution to polymer melting [12,13]. This was surprising since flexible, linear macromolecules should melt irreversibly [14]. Based on this observation the present, more detailed research on first-order transitions was begun. It involves the study of the first-order transitions of a broad range of small and large molecules [12,13,15–22] using heat flux calorimeters [23].

In TMDSC, a sample is heated with an underlying rate $\langle q \rangle$ and modulated by a periodically changing temperature. With sinusoidal modulation, the time-dependent sample temperature is:

$$T_s(t) = T_0 + \langle q \rangle t - \langle q \rangle \frac{C_s}{K}\left(1 - e^{-Kt/C_s}\right) + A[\sin(\omega t - \epsilon) + \sin\epsilon\, e^{-Kt/C_s}], \qquad (1)$$

where T_0 is the starting temperature; t the time; C_s the heat capacity of the sample calorimeter (pan plus sample); K the Newton's law constant; A the modulation amplitude; ω the modulation frequency ($=2\pi/p$, with p being the modulation period); and ϵ, the phase-lag relative to the heater temperature. The first two terms on the right-hand side of Eq. (1) represent the underlying increase of the heater temperature, $T_b = T_0 + \langle q \rangle t$. The third term results from the lag of the sample temperature behind the underlying temperature-increase of the heater (as in standard DSC [23]). The last term modifies the sample temperature by the chosen modulation, controlled at the sample thermocouple (TA Instrument MDSC™) or at the heating block (Mettler-Toledo ADSC™). Steady state is reached when the exponential terms in Eq. (1) approach zero. Changing the sinusoidal modulations to sawtooth modulations, the time-dependent sample temperature can be produced by linking a succession of the appropriately chosen first three terms on the right-hand side of Fig. 1, such that the required frequency and amplitude are produced.

The response to the heating program is seen in the change with time of the temperature difference

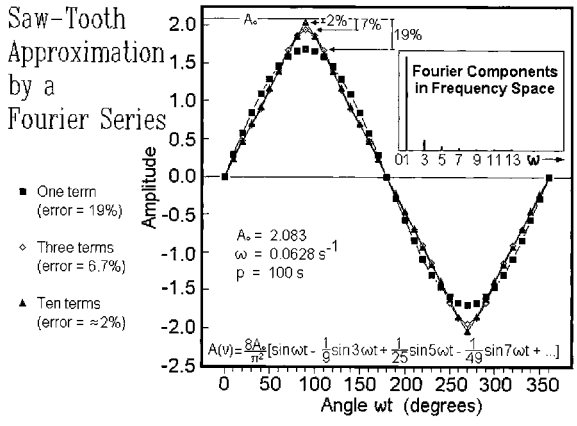

Fig. 1. Description of a quasi-isothermal saw-tooth by a Fourier series. The true maximum amplitude is given by A_0, $A(\nu)$ represents the change of A_0 as a function of the considered maximum numbers of harmonic contributions (ν=1, 3, 5, 7, etc.).

between the symmetrically placed reference and sample calorimeters. This temperature difference $\Delta T = T_r - T_s$, where T_r is the temperature of the reference calorimeter, is proportional to the heat-flow rate HF. For analysis, the periodic (reversing) part of the response at time t is separated from the raw data of the sample temperature, $T_s(t)$, and the heat-flow rate, $HF(t)$. This is to remove effects that are not caused by the modulation with frequency ω (such as the underlying heating rate and non-periodic losses and gains). The sliding average of $HF(t)$ over one period ($t \pm 1/2p$) is called the total differential heat-flow rate, $\langle HF(t) \rangle$. The value of $\langle HF(t) \rangle$ is in many applications identical to the result of the standard DSC and governed by the underlying heating or cooling rates $\langle q \rangle$. The difference between the calorimetric signal and the total heat-flow rate, $HF(t) - \langle HF(t) \rangle$, is the reversing "pseudo-isothermal" response at t caused by the modulation. This name is chosen since it applies to the modulation effect, corrected for the underlying change in temperature. In this paper it will be discussed on a number of examples how the evolution or absorption of a latent heat affects TMDSC. Latent heat is a heat that can be absorbed or evolved by the sample without changing its temperature. It will be shown that the study of the latent heat can be used to gain valuable insight into transition processes and their kinetics, as well as give a measure of calorimeter performance.

2. Experiments and computation

2.1. Typical instrumental details

A commercial Thermal Analyst 2920 system from TA Instruments with modulated DSC (MDSC™) was used with sinusoidal modulation. Its modulation is controlled by the sample thermocouple. Nitrogen gas with a flow rate of 10–30 ml min^{-1} was purged through the cell. Cold nitrogen, generated from liquid nitrogen was used for cooling. For the calibration of the heat-flow rate, sapphire was used. The pan weights were always about 23 mg and properly adjusted on the sample and reference sides. Detailed graphs of the limits of modulation as a function of temperature and cooling capacity were published earlier [4].

In the Mettler-Toledo DSC 820 (ADSC™), the temperature modulation is controlled at the heater thermocouple and is only little affected by the latent heats of the first-order transitions. The reference temperature T_r is calibrated relative to the furnace temperature, T_b. The temperature difference, ΔT, is determined by sensor plates with multiple-junction thermocouples. Dry nitrogen gas with a flow rate of 10 ml min^{-1} was purged through the cell. The cell base was purged with N_2 at 150 ml min^{-1}. The gas-flow rate was monitored and adjusted with a controller. The samples were weighed on a Cahn C-33 electrobalance to an accuracy of ±0.001% of the total load (50 mg). Both saw-tooth and sinusoidal modulations were carried out with this calorimeter.

Temperature calibration in the DSC mode was done for both instruments with the melting transitions of In (429.75 K), naphthalene (353.42 K), *n*-octane (116.4 K), acetone (177.9 K), cyclohexane (s/s 186.09 and s/l 297.7 K), cycloheptane (265.1 K), and Sn (505.05 K). The onsets of these first-order transitions were determined by extrapolation of the leading edge of the transition peaks to the baseline.

2.2. Data treatment

The recording, analysis, and deconvolution of the signals were done with the software of the chosen TMDSC, using the method described earlier [4]. The analysis of the raw data in the time domain is described as needed. The reversing heat capacity is extracted from the modulation amplitudes and given, for the case of equal mass of the empty sample and reference pans, by:

$$mc_p = \frac{A_\Delta}{A}\sqrt{\left(\frac{K}{\omega}\right)^2 + C'^2}, \tag{2}$$

with C' representing the pan heat capacity (equal for reference and sample); c_p, the specific heat capacity of the sample; m, the sample mass; and A_Δ is the modulation amplitude of the temperature difference ΔT (A_Δ is proportional to A_{HF}). The reversing heat capacity represents the absolute value of the complex heat capacity.

The experimental, reversing heat capacity when computed with the TMDSC software is:

$$mc_p = K_C \times \frac{\text{smoothed}\langle A_{HF}\rangle}{\text{smoothed}\langle A\rangle}, \tag{3}$$

where K_C is the heat capacity calibration constant, fitted to data from runs with sapphire [24] at the selected temperature, frequency, and pan weights, and given by:

$$K_C = C_p(Al_2O_3,\ \text{literature}) \times \frac{\text{smoothed}\langle A\rangle}{\text{smoothed}\langle A_{HF}\rangle} \tag{4}$$

with $\langle A\rangle$ and $\langle A_{HF}\rangle$ in Eq. (4) representing the calibration run. Comparisons of data of different frequency and/or reference-pan mass must be corrected according to Eq. (2), or calibrated with the correspondingly different values of K_C. Modeling software for the analysis of actual or assumed heat-flow rates with a simple spread sheet is available [25].

3. Results

3.1. Steady-state calculations for the saw-tooth

The most common temperature modulation is sinusoidal, as expressed by Eq. (1). It has the distinct advantage that it can be represented with only one term of the sum of the Fourier series:

$$T_s(t) - T_o - \langle q\rangle t = B_0 + \sum_{\nu=1}^{\infty}[A_\nu \sin(\nu\omega t) + B_\nu \cos(\nu\omega t)], \tag{5}$$

where A and B are coefficients that must be deter-

mined in the usual manner, and ν is an integer. As long as the modulation is centrosymmetric, B_ν=0 for all ν. For sinusoidal modulation only the first harmonic (ν=1) is found in the response of the heat flux calorimeter as long as there is no kinetic process within the sample that generates the higher harmonics. A typical example for the generation of higher harmonics is the glass transition [8–11]. The same is expected in response to sufficiently slow first-order-transition kinetics. The connection of Eqs. (5) and (1) at steady state, when $e^{-Kt/Cs} \rightarrow 0$, is obvious. As written above, A_1 in Eq. (5) is equal to A, all other A_ν are zero, and ωt in Eq. (5) corresponds to the phase lag of the sample temperature ($\omega t-\epsilon$) in Eq. (1).

The most frequently used non-sinusoidal modulation is the sawtooth. To generate a centro-symmetric sawtooth with an underlying heating rate $\langle q \rangle$ of 1.0 K min^{-1}, one can, for example, start with a heating rate of, let us say, 0.1 K s^{-1} (6 K min^{-1}) for 25 s. The subsequent cooling segment must then be 0.0667 K s^{-1} (4 K min^{-1}) for a duration of 50 s. This is followed by a full heating segment at 6 K min^{-1} for 50 s. The last two steps are then repeated to the end of the experiment. The period p for this saw-tooth modulation is 100 s, and the frequency is 0.01 Hz or ω=0.0628 rad s^{-1}. Subtracting the underlying increase in temperature from the saw-tooth leads to the pseudo-isothermal saw-tooth illustrated in Fig. 1. Its Fourier series is listed at the bottom of the figure. Using only the first term of the series as an approximation for the true sawtooth amplitude produces an error of about 20% in Eq. (2). A 5% error is reached with four terms of the Fourier series, but an error of 2%, as may be tolerable in C_p measurements, needs 10 terms. Similarly, the integral over time of the first harmonic of the heat-flow rate does not represent the actual heat exchanged. This rather negative assessment of the saw-tooth modulation does not agree with the good heat capacities that can be generated using only the first sinusoidal harmonics for the description of a sawtooth modulation of the temperature and the heat-flow rate response. The reason lies in the linear response of both, temperature and temperature difference to the modulation generated by the common heater. As long as this linearity is not disturbed by non-linear calorimeter design, electronic correction of the heater power, or sample properties,

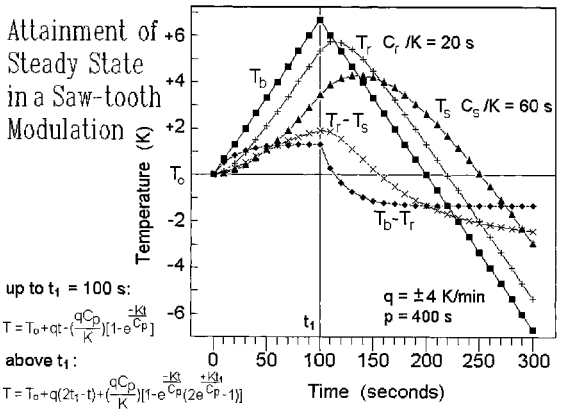

Fig. 2. Saw-tooth modulation in TMDSC (C_p in the equation represents either the heat capacity of the sample calorimeter or the reference calorimeter, i.e. C_r or C_s).

these deviations cancel since both, $\langle A_{HF} \rangle$ and $\langle A \rangle$ in Eq. (3) are equally affected. Note that a somewhat different discussion is necessary for power-compensated TMDSC where the temperature and heat-flow rate are governed by different heaters [26].

To explore the saw-tooth modulation further, a computation of the approach to steady state was carried out under quasi-isothermal condition [$\langle q(t) \rangle$=0]. Each segment of the saw-tooth was described by the first three terms of the right-hand side of Eq. (1). Two arbitrarily chosen values of C_p/K, represented each measurement. The smaller C_p/K is taken as the reference calorimeter (C_r/K), the larger one for the sample calorimeter (C_s/K). Fig. 2 illustrates the beginning of the saw-tooth modulation starting with $T_b=T_0=T(=T_r$ or $T_s)$. The temperatures are calculated under the condition of no temperature gradient within the calorimeters [25]. The approach to steady state beyond the first segment of the saw-tooth ($t>t_1$) is represented by addition of the solutions of the Fourier equation of heat-flow rate for termination at t_1 (which would lead at long times to $T=T_b=T_0+qt_1$) and initiation of the new saw-tooth segment [with the new steady state $T=T_0+q(2t_1-t)+qC_p/K$]. The saw-tooth modulation is particularly well suited to recognize the deviations from steady state in each segment [T_b, T_r, and T_s change with the same rate $\pm q$ and ΔT reaches a constant value $\mp q(C_r - C_s)/K$]. Clearly, T_r almost reaches steady state, while T_s and $T_r - T_s$ do not.

Figs. 3 and 4 show two examples calculated under conditions that attain and do not attain steady state,

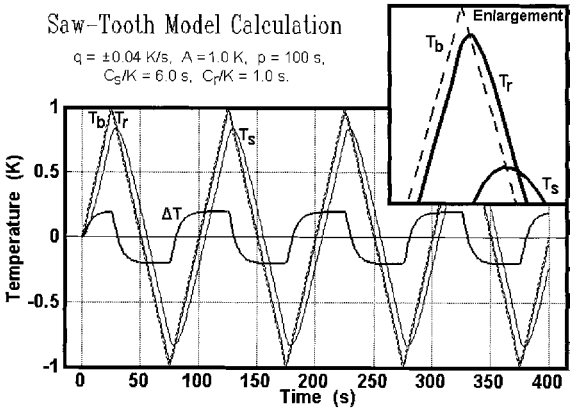

Fig. 3. Model calculations as in Fig. 2 for the case of attainment of steady state in each modulation cycle.

respectively. Table 1 is a collection of a larger number of calculations for different sample and reference calorimeters. Details of the calculation are given in the footnote to the table. The curves in Figs. 3 and 4 are repeating after the second cycle, but only the example of Fig. 3 attains steady state within each half-cycle, i.e., the proper heat-capacity input is recovered from a standard DSC calculation based on the horizontal portion of ΔT as shown in columns 3 and 4 of Table 1 (file nos. 5 and 9, respectively). The analysis using the first harmonics of the saw-tooth as given in Eq. (3) and used by the commercial software, and corrected for the different heating rate of the reference pan as given by Eq. (2), is given in columns

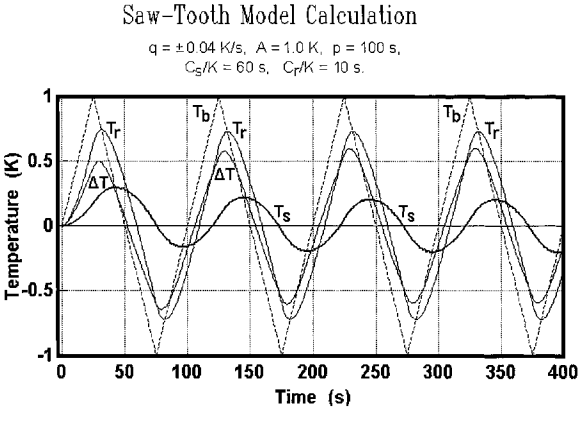

Fig. 4. Model calculations as in Fig. 2 for the case of no steady state, but note that after the second cycle the response is repeatable.

5–8, respectively. Even though steady state according to Eq. (1) is not reached in many cases, as soon as the cycles shown in Figs. 3 and 4 are repeatable, the reference-pan-corrected heat capacities give the proper values. Naturally, to transfer these calculations to actual experiments, there must be a negligible temperature gradient within the calorimeters, a rather stringent condition that is in need of further analysis. Special experiments to measure the true sample temperature are presently undertaken and the needed corrections for the power-compensated DSC which deviate from Eq. (2) have been developed [26].

3.2. First-order transitions

On going through a first-order transition, a much larger amount of latent heat must be handled by the calorimeter than is needed for a heat-capacity experiment over the same temperature range. A standard with a reversible and sharp transition is the melting and crystallization of indium. Its heat of fusion measures 3.29 kJ mol^{-1} at T_m=329.75 K and is absorbed over a temperature interval of less than 0.1 K [17,18]. In contrast, the heat absorbed due to heat capacity, is only 0.0268 kJ K^{-1} mol^{-1}. Over the temperature range of fusion, the calorimeter must, thus, conduct over 1000 times more heat for melting than is needed to raise the temperature due to the heat capacity of In. Present day calorimeters cannot handle such enormous changes in the heat-flow rate without lags. The kinetics of melting of In is sufficiently fast not to show significant superheating for the heating rates in typical scanning calorimetry [27].

In the standard DSC, one assumes that in the melting range the sample temperature remains fixed (at T_m) and a new steady state is reached that remains until melting is complete [23]. Fig. 5 illustrates how far this is possible [18]. Before and after the effects due to melting, the calorimeter is in a steady state corresponding to the heat-capacity-measuring mode (regions A and D, respectively). Actual melting occurs in the melting range (t_i to t_f) with an almost constant sample temperature (see the curves for T_s versus t and HF versus T_s). The recording of *HF* versus t must then have a leading peak edge that has the heating rate q as slope (area B in Fig. 5). The subsequent approach from the melting peak to steady state C supplies the

Table 1
Results of the calculation of heat capacity for saw-tooth modulation

File no.	$C_s/K-C_r/K$	$\Delta T/q$ (at max)	Deviation (%)	$(A_\Delta/A)/\omega$	Deviation (%)	Corrected	Deviation (%)
1	60−20=40	8.408	−79.0	24.908	−37.7	40.00	0
2	6−2=4	3.997	−0.07	3.969	−0.78	4.00	0
3	0.6−0.2=0.4	0.40	0	0.400	0	0.400	0
4	3−1=2	2.00	0	1.996	−0.20	2.00	0
5	6−1=5	4.997	−0.06	4.990	−0.20	5.00	0
8	10−1=9	8.866	−1.49	8.982	−0.20	8.00	0
7	30−1=29	9.468	−32.9	28.942	−0.20	29.00	0
6	60−1=59	22.655	−61.6	58.886	−0.19	59.00	0
9	60−10=50	14.916	−70.2	42.338	−15.3	50.00	0
10	60−5=55	19.181	−65.1	52.475	−4.59	55.00	0
11	60−2=58	21.817	−62.4	57.548	−0.78	58.00	0
12	60−0.2=59.8	23.425	−60.8	59.80	0	59.80	0

The heat capacities C_s and C_r, when divided by the Newton's Law constant K, are given in seconds, s; the linear heating and cooling rates of the saw-tooth q are 0.04 K s^{-1}; A, the amplitude set for the saw-tooth is ±1.0 K; the period p is 100 s; the frequency $\omega=2\pi/p=0.062832$ rad s^{-1}; at time $t=0$: $T_s=T_r=T_o$; C_p(standard DSC)/$K=\Delta T/q$; C_p(TMDSC)/$K=(A_\Delta/A)/\omega$; the correction factor for the TMDSC heat capacity is $[1+(C_r\omega/K)^2]^{1/2}$ (see Eq. (2)); the total length of analysis is 400 s, one point is calculated every second; for the standard DSC, ΔT is taken at the maximum or at the steady state of $\Delta T/K$; for the quasi-isothermal TMDSC the last 100 points of the first harmonic of the maximum modulation amplitude from a Fourier analysis were averaged (see Ref. [25]); t_x are the successive times of switches in heating and cooling at 0, 25, 75, 125, 175, 225, 275, 325, 375, and 425 s. Sample temperature during the heating or cooling cycle (subscripts: sample=s; reference=r):

$$T^1_{s,r} = T_{s,r}(t_x) \pm q(t - t_x) \mp (qC_{s,r}/K)[1 - \exp(-K(t - t_x)/C_{s,r})].$$

Approach to steady state after the switch from heating to cooling and vice versa (at $t=t_x$):

$$T^2_{s,r} = (\pm A \mp T_{s,r}(t_x))[1 - \exp(-K(t - t_x)/C_{s,r})],$$

(T^1 and T^2 are the appropriate solutions of the heat-flow rate equation, as given in [23], compare also to Eq. (1)). The total response to the saw-tooth modulation is, thus:

$$T_{s,r}(t) = T^1_{s,r}(t) + T^2_{s,r}(t).$$

delayed heat capacity contribution due to the constant T_s during melting and corrects for different heating rates of sample and reference in B [23].

Fig. 6 displays the melting of indium with sinusoidal temperature modulation [18]. The melting peaks (A and C) and the intervening crystallization peak (B) are well separated and steady state is reached after each of the transitions. During the first melting, the sample temperature drops slightly after the onset, in accord with the decreasing heating rate as one approaches point d. On cooling, the onset of crystallization has a supercooling of 1.2 K (peak B) because melting in the prior cycle was complete so that crystal growth requires nucleation. Once nucleated, the heat of crystallization is, however, released sufficiently quickly to increase the sample temperature to within 0.1 K of the minimum of T_s at d. The second melting, C, occurs during the almost linear increase in the sinusoidal temperature program at the maximum heating rate of 7.3 K min^{-1}. The isothermal segment shows a higher sensor temperature of about 0.25 K, in agreement with the calibration of T_m as a function of heating rate by standard DSC ($dT_m/dq \approx 0.03$ min) [17].

The variations of the sensor temperature of the sample during melting indicate the need of assessment of the causes of lags due to latent heat in addition to the absolute temperature calibration. The integration of heat-flow rate for the individual melting and crystallization transitions in sinusoidal TMDSC is more difficult than in standard DSC because of the sinusoidal "baseline," but TMDSC allows a better assessment of the reversibility of the transition, a valuable addition to calorimetric analyses. Quantitative heats of

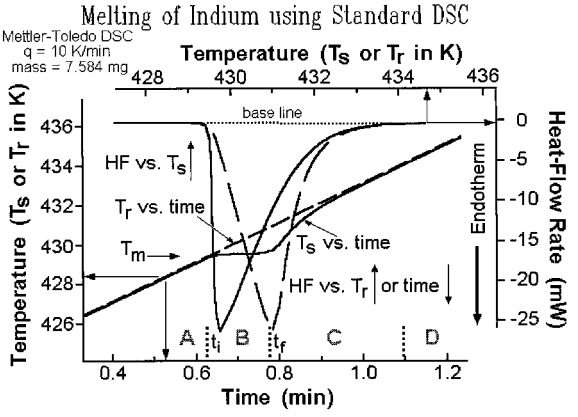

Fig. 5. Changes of temperatures and heat-flow rate during the melting of indium using standard DSC.

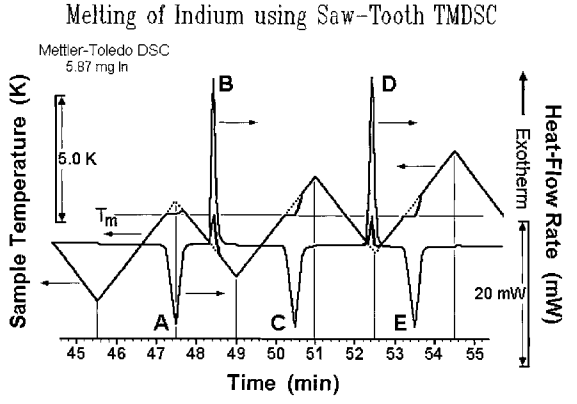

Fig. 7. Saw-tooth modulation for TMDSC showing the melting of In. Heating and cooling segments with rates of change of 2.0 K min^{-1}. Two minute heating segments are followed by 1.5 min cooling segments to give an underlying heating rate of 0.29 K min^{-1}.

the transition are, naturally, better obtained by standard DSC.

Fig. 7 illustrates a similar experiment with saw-tooth modulation. The modulation conditions lead to three melting steps (A, C, and E), separated by two crystallizations (B and D). The figure shows elements of both, the standard DSC of Fig. 5 (peaks B, C, and E) and the changes in heating rate of the sinusoidal TMDSC of Fig. 6 (peaks A and D). The saw-tooth experiment has two advantages over sinusoidal modulation, namely the detection of steady states is elementary and the extrapolation of baselines involves straight lines.

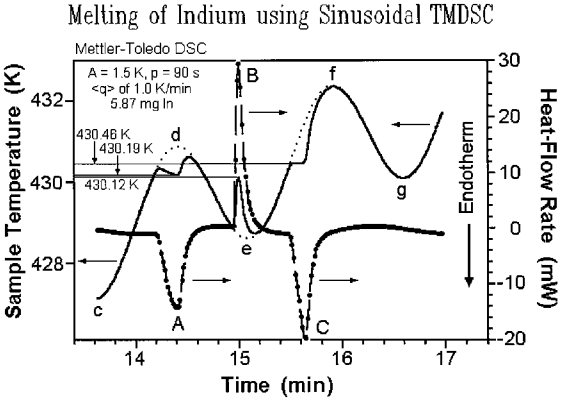

Fig. 6. Melting of indium on TMDSC. The dotted lines mark the undistorted sinusoidal sample temperatures.

The response of TMDSC during first-order transitions is further demonstrated on a number of examples with different features:

1. A close-to-reversible transition in pentacontane ($C_{50}H_{102}$) [19]. Pentacontane has a somewhat broader transition region and a large heat of transition and, as for most organic materials much lower thermal conductivity.
2. A reversible and sharp transition in the liquid-crystal-forming 4,4′-azoxyanisole [20–22] which has a much smaller heat of transition. For comparison with indium, the effect of its smaller thermal conductivity may be compensated by the smaller heat of transition.
3. Several polymeric mesophase transitions which may range from reversible to irreversible and have small to large heats of transitions [20–22].
4. A fully irreversible first-order transition of well-crystallized poly(oxyethylene) (POE) [15,16].
5. Several combinations of transitions that combine reversible and irreversible effects, as are common in poorly crystallized, nanophase-separated polymers such as poly(ethylene terephthalate) (PET) [12,13], POE [15,16], poly(trimethylene terephthalate) (PTT) [28], and poly(ethylene-*co*-octene) (PE/PO) [29,30]. These polymers have relatively large, irreversible heats of transition, with superimposed, time-dependent, partially or fully reversible processes of not fully understood nature.

The details of each of these five types of transition behavior are too extensive to be described here in detail, but should be looked-up in the given references. The key issues, however, are discussed on hand of selected figures.

4. Discussion

4.1. Saw-tooth heat capacity

Figs. 8 and 9 represent the heat-flow rate analysis of Figs. 3 and 4, respectively, for a cycle that has become repeatable. The first, third, and fifth harmonic are drawn and allow to assess the changes in the actual signals when representing them by the first harmonic only. As long as the calorimeter response is fully governed by a heat flux described by Newton's law, the symmetry of the saw-tooth or sinusoidal modulation of the heater temperature is carried to the sample temperature and the heat-flow rate, even in the process of approach to steady state, i.e., the even harmonics are zero. As soon as the response is electronically corrected, however, this may not be so, pointing to the importance of complete disclosure of signal generation and treatment by manufacturer as well as experimenter. Perhaps for these reasons could we obtain to date only qualitative matches of experiments with Eq. (1)[31].

Fig. 8 depicts the case when steady state is also reached within each linear portion of the saw-tooth,

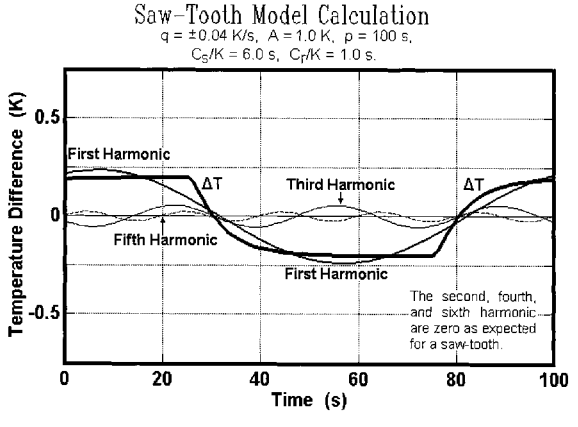

Fig. 8. Analysis of one cycle of the saw-tooth modulation computed in Fig. 3 after repeatability was reached.

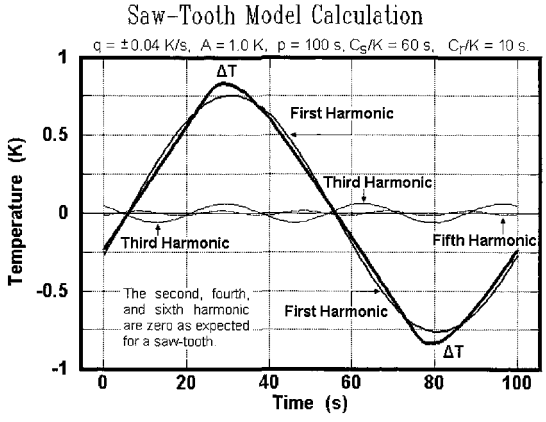

Fig. 9. Analysis of one cycle of the saw-tooth modulation computed in Fig. 4 after repeatability was reached.

whereas Fig. 9 illustrates the case when such steady state is not reached (Fig. 8 corresponds to entry no. 5 of Table 1, Fig. 9, to no. 9). The difference in heat capacity between sample and reference calorimeters, normalized by the Newton's law constants, $(C_s - C_r)/K$, can be calculated from the standard DSC response (Table 1, column 3) and the reversing TMDSC response (Table 1, column 5). The DSC analysis fails as soon as steady state cannot be achieved within each half-cycle, while the TMDSC analysis, making use of only the amplitudes A of the first harmonic of the Fourier representation of the response still gives precise answers (column 7) as long as one does not use the uncorrected Eq. (3) (column 5). This surprising result is linked to a compensation of errors due to the linear response of the heat-flux calorimeter for the numerator and denominator of Eqs. (2) and (3). The same is expected for sinusoidal modulations. This advantage of measurement without reaching or maintaining steady state gives, however, not a license to increase sample mass, modulation amplitude and frequency to maximize the calorimeter response. The remaining severe condition for quality measurements is a negligible temperature gradient within the sample, not considered in the calculations for Table 1. Again, it must be emphasized that the use of Eq. (3) in power-compensated TMDSC needs a different, mass-dependent, correction factor [26].

The importance of the discussion of heat capacities in this paper dealing with transitions lies in the possibility that a broad transition may be analyzed

as an "apparent heat capacity." The integral of the apparent heat capacity over the transition region should give the heat of transition, when corrected by the expected enthalpy arising from the known true heat capacities. The latter are often available from the ATHAS data bank [32,33], or can be extrapolated from outside the transition region. Naturally, one can expect reliable data only if true heat capacities of the same magnitude as the apparent heat capacity can be measured reliably under similar conditions of measurement on a sample that does not show such transitions. Kinetic information can also be extracted from the frequency dependence of the apparent heat capacity if true heat capacities of similar magnitude give constant values under the same conditions [34–36].

4.2. Indium

The TMDSC of In is discussed based on [17,18]. Fig. 10 is similar to Fig. 6, but with a much slower underlying heating rate of 0.1 K min^{-1}, so that seven melting and six recrystallization peaks can be observed. The melting peaks 1–5 are incomplete, i.e., after the sample temperature drops below the melting point, crystal nuclei remain. As a result, the corresponding crystallizations 1′–5′ are continuous with the interruption of melting since there are sufficient nuclei to make the transition reversible. The cross-over from endotherm to exotherm occurs close to the equilibrium melting temperature T_m. Since in

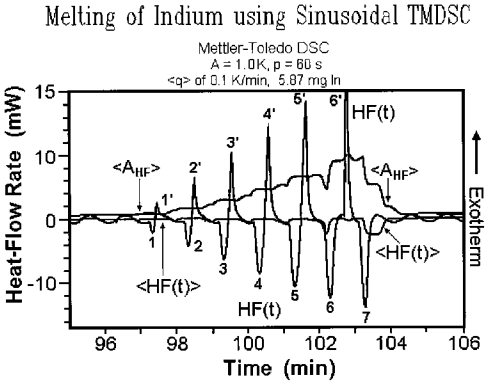

Fig. 10. Heat-flow rates during the melting of indium as in Fig. 6, but with a lower underlying heating rate and changed modulation parameters.

separate, quasi-isothermal experiments it was proven that the melting range of In is narrower than ±0.05 K and the melting rate is known to be fast [27], the breadth of the melting peaks is caused by calorimeter lag. There is not enough time to conduct sufficient latent heat into the sample for complete melting over the narrow equilibrium-melting range. When recording 1/1′–5/5′, the sample must have had a portion of unmelted indium in the center of the pan with melt contacting the bottom, sides, and (depending on the degree of filling of the pan) also the top. Each successive modulation cycle melts more of the In, as can be seen from the increasing size of the crystallization peaks 1′–6′. Only after peak 6 is melting complete and supercooling for nucleation is needed for peak 6′ and after peak 7 the supercooling is not reached by the nucleation anymore. While the chosen TMDSC parameters of Fig. 6 permitted the completion of regions A–D of Fig. 5, they could not be completed without overlap in the experiment of Fig. 10.

The total heat-flow rate $\langle HF(t)\rangle$ due to melting is almost constant up to peak 7. It shows small, but increasing amounts of excess melting (endotherms) for each cycle because each melting peak exceeds the prior crystallization peak (1′<2–5′<6). The endotherms are, furthermore, broadened due to the averaging over $\pm 1/2p$. The final peaks 6′ and 7 are of equal magnitude and since no further crystallization occurs beyond melting peak 7, all remaining heat of fusion is recorded as soon as it is not compensated by the prior crystallization, i.e., the main melting peak in $\langle HF(t)\rangle$ is completed only p seconds after crystallization has ended. Overall $\langle HF(t)\rangle$ of TMDSC has under such conditions little in common with the melting peak of the standard DSC (see Fig. 5).

Trying to derive an apparent, reversing heat capacity from Eq. (3) using the heat-flow-rate amplitude $\langle A_{HF}\rangle$ of the first harmonic of a Fourier series for $HF(t)$ leads to excessively large values, as shown in Fig. 10. The larger the number of melting and crystallizations, the larger is the detected area under the heat-flow-rate amplitude. Neither do these values represent the true amplitude (because of the non-sinusoidal shape) nor can the ratio with A be trusted to give a correct apparent reversing heat capacity (because A depends on the temperature gradient that develops between the sample, which in its center is close to T_m and not modulated, and the sample-temperature sensor which

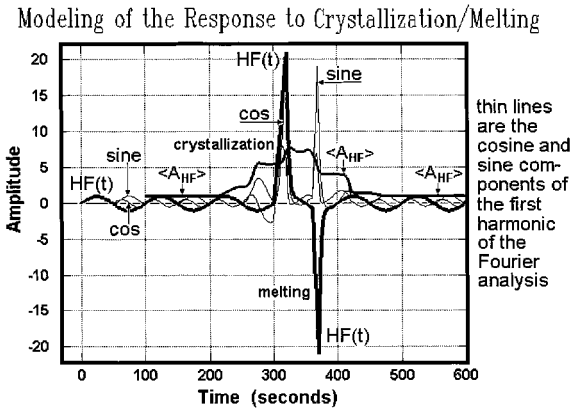

Fig. 11. Model calculation of a single crystallization, followed by final melting using the software generated in [16]. To be compared with peaks 6′ and 7 of Fig. 10.

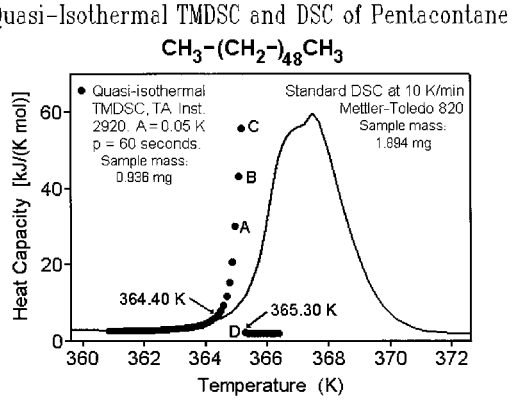

Fig. 12. Heat capacities of pentacontane by standard DSC and quasi-isothermal TMDSC computed from Eq. (3).

is under the influence of the heater modulation). Fig. 11 shows how well a model calculation of the last two peaks in Fig. 10 agrees with the experiment. The figure indicates also the various components of the Fourier analysis. Attempts to analyze the progress of melting by calculation of the apparent reversible heat capacity give, thus, quite erroneous results. In this case only a direct analysis of the raw signal is possible, as was given in Figs. 6 and 7 (see also Figs. 13–15, 17 and 21, below).

4.3. Pentacontane

Pentacontane, $C_{50}H_{102}$, has a somewhat broader melting transition than In, still a rather high heat of fusion, but the much lower thermal conductivity of organic materials. Its thermal behavior is probed in [19]. Fig. 12 shows a comparison of the apparent heat capacities gained by quasi-isothermal TMDSC and standard DSC. Because of the needed higher precision in temperature for the discussion, the different calorimeters were calibrated to the melting point of $C_{50}H_{102}$ observed by optical microscopy (365.30±0.05 K). The beginning and end of melting by TMDSC are marked in Fig. 12 and leads to an overall melting range of about 1.0 K. The running sum of all the endotherms and exotherms of the quasi-isothermal experiments including the 0.10 K steps between successive measurements was determined. Up to 365.20 K (point C) the sum reached only 34% of the total melting, i.e., most melting occurs in going to and measuring at 365.30 K (point D). During the final modulation cycles at D, the sample melts completely. Up to point C the modulation response gives a practically reversible apparent heat capacity and the net melting occurs mainly in the 0.1 K jumps to the next point of measurement. The standard DSC at a heating rate of 10 K min^{-1} has a comparable breadth of melting peak as found for In in Fig. 5, but the indicated T_s does not keep constant temperature, indicating a bigger instrument lag.

Fig. 13 illustrates the Lissajous figures of the heat-flow rate versus sample temperature for points A–D of Fig. 12. At temperatures A–C the small deviation from true ellipses indicate that the apparent heat capacities vary during the modulation cycle, but are otherwise largely reversible. In going to point D, 66% of the total heat of fusion is absorbed. One can see that in every cycle more paraffin melts than crystallizes. Finally, the Lissajous figure settles into the shape for the stable melt. This occurs when all crystals melted and new crystal nucleation would be needed for crystallization.

The kinetics of the melting and crystallization process could in this case be followed, but it is probably difficult to separate the crystal melting rate from the limits set by the thermal conductivity of the melt surrounding the remaining crystal. From the cross-over between crystallization and melting in Fig. 13, one can estimate the end of melting to be somewhat less than 365.30 K, the calibration point set by optical microscopy.

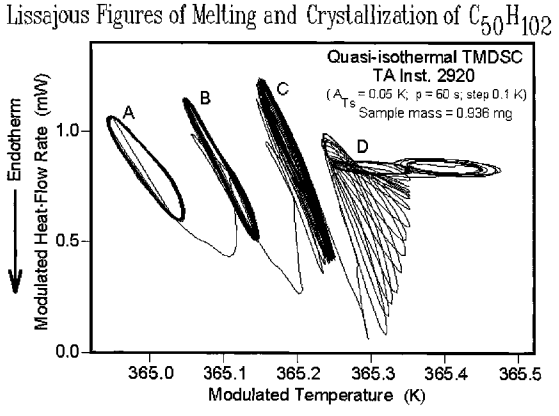

Fig. 13. Lissajous figures of pentacontane at the indicated points of Fig. 12.

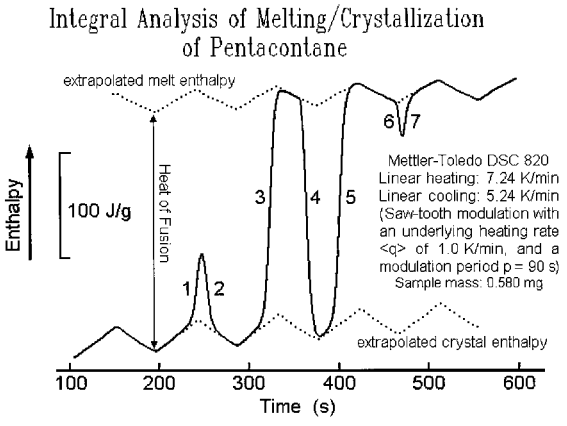

Fig. 15. Integral analysis of Fig. 14.

Fig. 14 illustrates TMDSC with saw-tooth modulation for pentacontane. The dashed curve represents the raw data of the heat-flow rate, $HF(t)$. It increases strongly in the melting and crystallization regions of the paraffin. The solid curve represents the sample temperature, $T_s(t)$. In the melting and crystallization regions, it deviates from the expected (dotted) program of sawtooth modulation because of the absorption and evolution of the latent heat. Odd numbered peaks mark the melting and even numbers, the crystallization. The onset of melting and crystallization between peaks 3–5 agree within 0.4 K.

Using an integral analysis, as shown in Fig. 15, one can get clear information about the degree of completion of the transition for each cycle. The solid curve was obtained by integrating the heat-flow rate in Fig. 14. The dotted curves are extrapolations from the integral data before and after the transition regions. Just measuring the height of the enthalpy gives an answer of how much crystal melts and how much melt crystallizes in each segment of the saw-tooth. The bottom dotted curve represents the enthalpy of the crystalline paraffin and the top dotted curve the enthalpy of the melted paraffin.

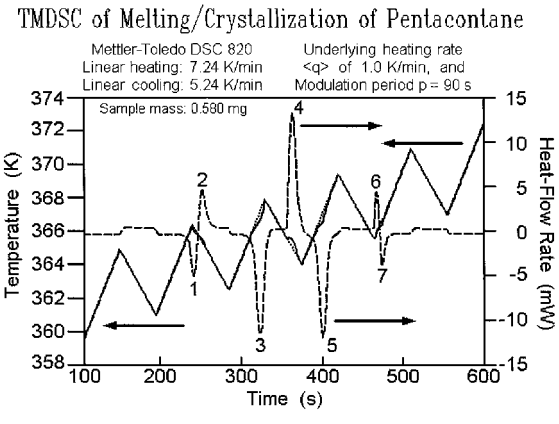

Fig. 14. Saw-tooth analysis of the melting of pentacontane.

4.4. 4,4′-Azoxyanisole

Fig. 16 and 17 illustrate a reversible and sharp transition of the liquid-crystal-forming 4,4′-azoxyanisole [21] which has a much smaller heat of transition than indium or pentacontane. The quasi-isothermal results (●) document that the apparent heat capacity of the 4,4′-azoxyanisole gradually increases on approaching the transition temperature from the low-temperature side, as is common for LCs. Close to the onset of isotropization measured with the traditional DSC (407.93 K) a large jump occurs in the quasi-isothermal TMDSC, as expected for a sharp first-order transition. The width of the main transition can be estimated from the step-width of the quasi-isothermal runs to be about 0.2 K.

The reversible, apparent heat capacity of the standard TMDSC of Fig. 16 is much broader than the quasi-isothermal measurement in the same figure. The main reason for this peak broadening is the larger modulation amplitude (A =0.5 K) over which is averaged when evaluating $\langle A \rangle$ and $\langle HF \rangle$ for Eq. (3). With an underlying cooling rate (dotted curve of Fig. 16),

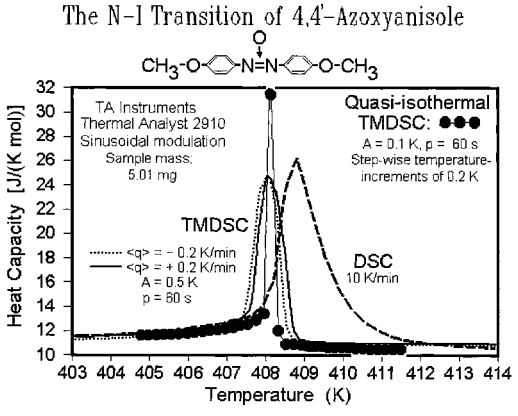

Fig. 16. Analysis of the nematic-liquid-crystal/isotropic-melt transition of 4,4′-azoxyanisole.

practically identical curves to heating result, supporting the fact that the transition is an equilibrium transition. The small shifts between heating and cooling curves are caused by the change of the transition temperature with the underlying heating rate.

From the reversing heat capacity of the standard TMDSC in Fig. 16 (solid and dotted lines) one cannot evaluate a heat of transition because the reversing heat-flow rate represents only the first harmonic of the Fourier series as, shown in Fig. 11, and multiple peaks will falsify the integration. One can, however, integrate the heat-flow rate in the time domain, as illustrated for the pentacontane in Fig. 15. The heat of isotropization of the nematic phase for 4,4′-azoxyanisole determined by this method is 2.56 J g^{-1}, which agrees well with the value obtained from the traditional DSC (2.52 J g^{-1}).

Fig. 17 illustrates the heat-flow rate in TMDSC as a function of time and temperature controlled at the furnace, not at the sample and with a much larger modulation amplitude. The initial, partial isotropization, followed by partial ordering occurs on the fifth cycle and attains full conversion from the ninth cycle to the 12th cycle. This is supplanted by decreasing conversion. Complete liquid response is acquired with the 16th cycle. Again, one finds that it takes about 0.4 K to traverse the transition (4 cycles $\times$ $\langle q \rangle$ $\times$ p). The deviation of the heat-flow rate from a sinusoidal response is obvious from Fig. 17. The broadness due to the instrument effect, in turn, can be taken from a Lissajous figure versus temperature to be about 1 K, similar to the results of Fig. 16 [21].

Liquid crystals with flexible appendages, such as N,N′-*bis*(4-*n*-octyloxybenzal)-1,4-phenylenediamine have a similarly small heats of transition, but show a broadening of the transition to about 3 K. In this case DSC, TMDSC, and quasi-isothermal TMDSC become identical [20–22] (see also Fig. 18, below).

4.5. Polymeric mesophases

Broad, reversible transitions are also observed for liquid crystalline polymers. Fig. 18 depicts in the

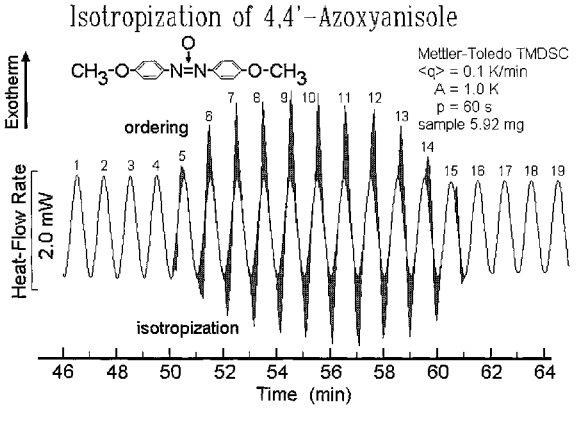

Fig. 17. Details of the heat-flow rate for a TMDSC analysis of 4,4′-azoxyanisole.

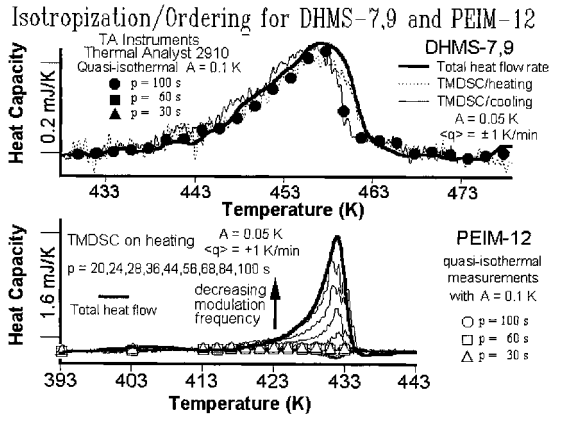

Fig. 18. Comparison of the isotropization/ordering of polymeric liquid crystals and conformationally disordered crystals by TMDSC.

upper figure the nematic/isotropic transition of a polyether, synthesized by coupling 4,4′-dihydroxy-α-methylstilbene with a 1:1 molar mixture of 1,7-dibromoheptane and 1,9-dibromononane (DHMS-7,9, with a nematic phase between 400 and 470 K [20]). The molar mass of DHMS-7,9 is 36 000 Da. The broadness of the transition is now about 20 K, sufficient to treat the complete transition as an apparent change in heat capacity. All three analysis methods give practically the same result, i.e., the reversing, apparent heat capacity from both quasi-isothermal and with an underlying heating rate correspond to the apparent heat capacity from the standard DSC.

Of great importance is the observation that macromolecules may also exhibit a completely different mesophase, that of a conformationally disordered phase [37]. Overall studies of this phase reveal that conformationally disordered crystals are more closely related to true crystals than to melts and, thus, should be more irreversible in their transition behavior, i.e., show a supercooling before ordering [14]. The lower curves in Fig. 18 show the TMDSC results for the melting transition of the condis crystals of poly(4,4′-phthaloimidobenzoyldodecamethyleneoxycarbonyl) (PEIM-12). Quite clearly the transition does not show in the quasi-isothermal TMDSC, and TMDSC runs with an underlying heating rate also have no contribution if the frequencies are sufficiently high. After appropriate correction for the phase shift due to the increased heat-flow amplitude [38] and deconvolution from possible instrument lags, it may be possible in this case to extract transition-kinetics information from the frequency dependence [34–36]. Problems may arise from such analyses when melting is coupled with crystal perfection, a common observation in polymers [14].

4.6. Irreversible first-order transitions

The study of melting and crystallization of flexible macromolecules (polymers) by adiabatic and differential scanning calorimetry has ascertained over the last 40 years that this process is fully irreversible. Typical supercooling of polymer melts are 5–15 K, far more than covered by typical modulation amplitudes [14]. Fig. 19 proves this fact for well-crystallized poly(oxyethylene) with a molar mass of about 5000 Da (POE 5000) [15,16]. No latent heat of the

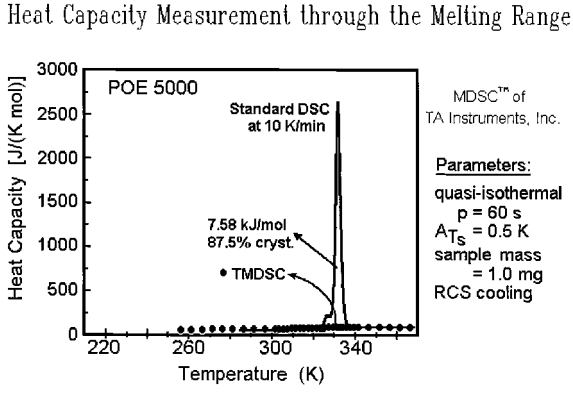

Fig. 19. Irreversible melting of poly(oxyethylene).

sharp and large melting peak shows in the quasi-isothermal results. Melting is fully irreversible and occurs only when raising the temperature from one quasi-isothermal run at to the next. Later in each run, when data are taken for the reversing heat capacity analysis, no melting/crystallization contributions are apparent.

Repeating the same experiments with less-well crystallized samples of lower molar mass (POE 1500), the sample shows a small amount of excess apparent heat capacity in the melting region, as illustrated by Fig. 20 [15,16]. More careful crystallization eliminates this small peak. To identify the reversible effect within the polymeric materials, an analysis with varying modulation amplitudes was carried out. Fig. 21 shows the result. At the lower modulation amplitudes the Lissajous figures indicate a normal

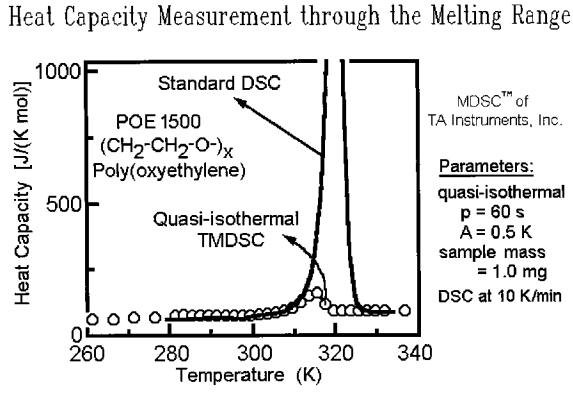

Fig. 20. Observation of a small amount of apparent reversing heat capacity of POE.

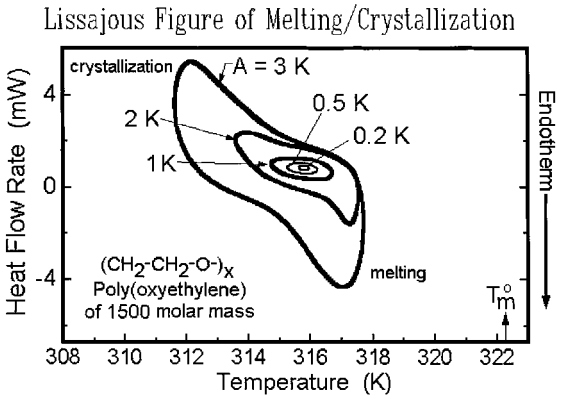

Fig. 21. Lissajous figures for the sample of Fig. 20 for different modulation amplitudes at 315.6 K.

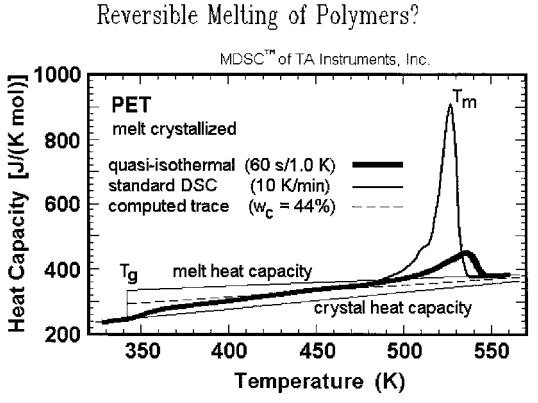

Fig. 22. Observation of a small amount of apparent reversing heat capacity in a semicrystalline poly(ethylene terephthalate).

reversing heat-flow rate without melting and crystallization. For A=2.0 K, melting and crystallization can be seen, i.e., the modulation has bridged the zone of metastability between crystallization and melting. Since the equilibrium melting temperature is, as indicated in the figure, still not covered by the modulation, this experiment can be used to study the limited crystal perfection when growth occurs at the indicated crystallization temperature. From the earlier onset of crystallization than expected from the modulation with smaller amplitude, it can be concluded that melting is incomplete and leaves nuclei to enhance crystallization. Furthermore, since the modulation period was constant, one can deduce that the crystals, once grown, perfect continually. At A=3 K the time between last crystallization and first melting is less than at A=2 K, and the melting temperature is lower. By changing amplitude, frequency, and base-temperature, T_0, the melting-crystallization-perfection diagram could be studied to resolve questions of molecular nucleation [39,40].

4.7. Nanophase-separated polymers

Two more observations have been made on observing the usually poorly crystallized high- molar-mass polymers, namely, a small reversible contribution to the melting peak, and an increase of the heat capacity before melting. The first of these effects was first seen for poly(ethylene terephthalate) (PET) [12,13]. Later, similar effects were observed for a high-molar-mass POE [15,16], poly(trimethylene terephthalate) (PTT) [28], and poly(ethylene-*co*-octene) (PE-PO) [29]. The main points are summarized on the examples of PET and PE-PO.

Fig. 22 is a reprint of the figure first shown at the 4th Lähnwitz seminar [7]. The quasi-isothermal TMDSC senses only a small portion of the overall melting of a typical melt-crystallized, semicrystalline PET. Its melting peak is shifted to somewhat higher temperature due to the prolonged experimentation at each temperature, T_0 (20 min every 2 K). More details and a comparison to an initially amorphous PET are shown in Fig. 23. Proof could be brought that this effect is not instrument dependent or modulation induced [41]. From the frequency dependence of the increase of the reversing heat capacity at the glass transition the

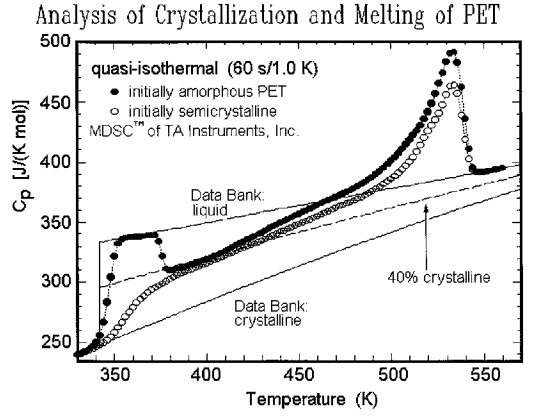

Fig. 23. Comparison of TMDSC of initially amorphous poly(-ethylene terephthalate) to the data of Fig. 22.

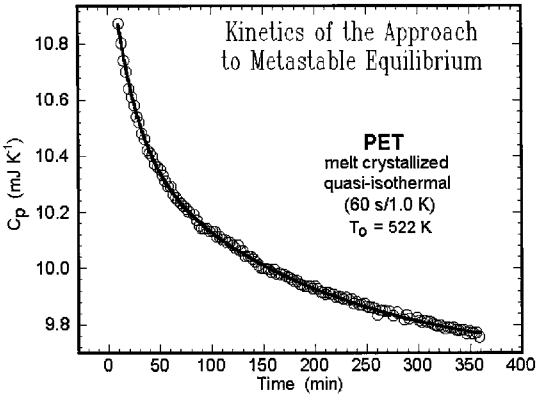

Fig. 24. Time-dependence of the apparent reversing heat capacity for a semicrystalline poly(ethylene terephthalate).

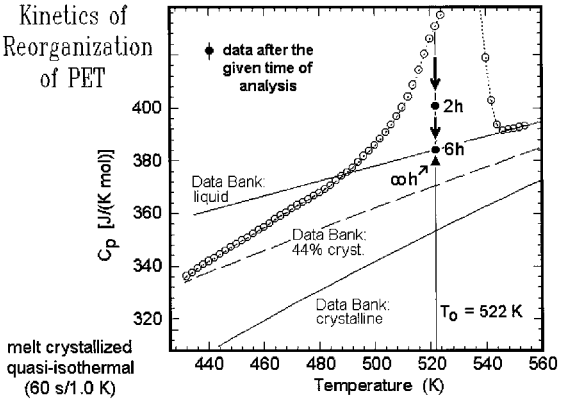

Fig. 25. Comparison of the data in Fig. 24 with the heat capacities of Fig. 23 and extrapolation to infinite time.

kinetic parameters of PET could be derived [10,11]. Similarly, one could derive the slow kinetics of the fully irreversible (non-modulated) cold crystallization from the kinetics of the decrease of the reversing heat capacity from the amorphous to the semicrystalline value. From the difference between the apparent reversing heat capacities of the two samples one sees that crystal perfection decreases the reversing contribution to the heat capacity.

Further information on the nature of the reversing contribution to melting was obtained by long-time experiments, as shown in Fig. 24. Obviously the reversing apparent heat capacity is not an equilibrium value, but decreases with time. A check of the ultimate value obtained in comparison to the expected heat capacities is shown in Fig. 25. This series of figures can be interpreted such that melting produces a surface layer on the crystals which can recrystallize without molecular nucleation [14,39,40]. Furthermore, with time this surface layer reorganizes and reaches a steady state with a minimum of reversible melting. For PET the first surface melting seems to be observable at about 415 K (see Fig. 23). These observations indicate an important step in the elucidation of the properties of polymer crystals and present a new tool to further analyze the kinetics of reorganization as well as melting.

Increasing the poorly crystallized polymer by copolymerization enlarges the locally reversing contribution to the apparent heat capacity. Fig. 26 illustrates this large-scale reversibility on the example of poly(ethylene-*co*-octene) [29,30]. The sample is a commercial, metallocene-catalyzed copolymer (ENGAGE™ 8200) with 24 wt% octene and a molar mass of approximately 78 000 Da. Fig. 26 shows also the heat capacity of amorphous and crystalline polyethylene as documented in the ATHAS data bank [32][3] (open and filled symbols, respectively). The reversing heat capacity measured by TMDSC (thick lines) is furthermore compared to the apparent heat capacity measured by standard DSC (thin lines). The experimental values below the glass transition (237 K [42]) and for the melt they agree well with the data bank. During heating, the melting process seems to start at 240 K, i.e., imme-

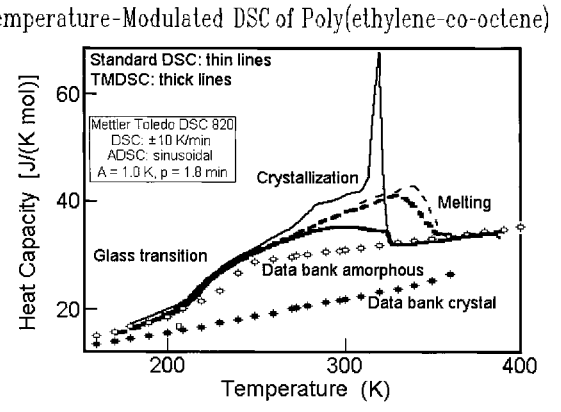

Fig. 26. Analysis of poly(ethylene-*co*-octene) by DSC and TMDSC. Sample mass 10 mg. Heating is indicated by the dashed lines and cooling by solid lines.

[3]For data and further information see our web site (URL: http://web.utk.edu/~athas).

diately above the glass transition, and is finished at 355 K (end of melting). The crystallinity is 24% at 240 K and decreases continuously to a value of 14% at 298 K, assuming the heat of fusion is the same as for a perfect crystal – 4.1 kJ (mol of CH_2)$^{-1}$ at the equilibrium melting temperature of 414.6 K [43]. The crystallization process during cooling begins at 323 K and covers the temperature range down to the glass transition. The crystallization consists of at least two different processes, indicated by the sharp peak at 318 K (maximum) and a more continuous process afterwards. The discrete peak at the beginning of the crystallization only appears in the total heat capacity, not in the reversing heat capacity, i.e. this process is non-reversible and continues to about 255 K. However, at approximately 328 K the reversing heat capacity also increases as a result of a second exothermic process which continues over a wide temperature range. This observation contrasts the more frequently seen completely non-reversing character of crystallization, especially if the process occurs over a narrow temperature range. The heating scan supports the assumption of a continuous melting above the glass transition and appears mainly in the reversing component of the heat-flow rate. Larger deviations between the underlying and reversing heat capacity can be seen in the end of the melting process as a separate shoulder. It is straightforward to assume that this melting (with a different kinetics than the continuous melting at lower temperatures) is correlated to the crystallization characterized by a corresponding kinetics, i.e., the first crystallization peak. Time-resolved X-ray diffraction provided proof of two different crystal structures in the copolymer (hexagonal and orthorhombic) [29,30].

5. Conclusions

1. The modeling of TMDSC with a saw-tooth-like temperature-change provides evidence that as long as there is a negligible temperature gradient within the sample and the Fourier equation of heat-flow rate governs the experiment, Eq. (2) describes the heat capacity (Figs. 1–4, 8, 9). This equation holds, as shown in Table 1 even though the first harmonic amplitudes of the sample temperature and heat-flow rate do not reach steady state. Any alteration of the heat-flow rate by electronic controls, as are often applied in TMDSC, would destroy the linearity of the differential measurement and need to be checked experimentally. Similarly, temperature gradients within the sample are in need of analysis as becomes obvious from the study of first-order transitions.
2. The key variables TMDSC of the first-order transitions are:
   - The width of the transition region which may vary from less than 0.05 K (In) to more than 100 K (polymers).
   - The heat of transition which may differ by more than a factor of 100 in going from crystal/liquid to LC/liquid and crystal/crystal transitions.
   - The thermal conductivity which varies by a factor 1000 in going from polymers to metals.
   - The reversibility of the transition, which may vary from fully reversible (In, when nucleated and LCs) to fully irreversible (polymers) and have many intermediate and overlapping cases (specifically in nanophase-separated, semicrystalline polymers).
3. On the hand of several examples (Figs. 5–7, 10–26) many of the variables were tested. The data on the reversible, sharp melting, high heat of transition, and high thermal conductivity of indium (Figs. 5–7) can serve as a test substance for the performance of the calorimeter. An analysis with an ''apparent heat capacity'' using a partial Fourier analysis as given by Eqs. (3) and (4) is impossible (Figs. 10 and 11). Analyses in the time domain, on the other hand can be done as long as the different zones of different steady state and approach to steady state (A–D in Fig. 5) do not overlap between successive modulation cycles. Of special value for the analysis in the time domain is the integral analysis demonstrated in Fig. 15. The same limitations as for In apply to the reversible isotropization transition for 4.4′-azoxyanisole which compensates the lower thermal conductivity with a lower heat of transition (Figs. 16 and 17). The paraffin pentacontane with its increased heat of transition illustrates the problems of high heat of transition, close to reversible transition, and low thermal conductivity (Figs. 12–15). For polymers, irreversibility of melting is the major property. Only the

rare polymeric LCs seem to be able to be fully reversible. Due to their low heat of transition and broad transition region the ''reversible apparent heat capacity'' can be used to study the transition (Fig. 18). Fully irreversible melting (Fig. 19) and the newly discovered two types of locally reversible surface structures (Figs. 20–25) are displayed. Finally an example of the characterization of a sample with almost equals fractions which behave reversibly and irreversibly is illustrated in Fig. 26.

4. It is shown that TMDSC presents a valuable tool for the study of first-order transitions. Such analyses must deal, however, with a broad range of variables and special steady states so that care must be taken to separate the transition properties from delayed calorimeter response. Of particular importance is to realize that a large latent heat may lead to a portion of the sample being isolated from the modulation of the melt by its surface that remains at the transition temperature. Future works on assessing temperature gradients within the sample by contact-free IR thermometry are underway and may be a topic for the Sixth Lähnwitz Seminar in the year 2000.

Acknowledgements

This work was supported by the Division of Materials Research, National Science Foundation, Polymers Program, Grant no. DMR-9703692 and the Division of Materials Sciences, Office of Basic Energy Sciences, US Department of Energy at Oak Ridge National Laboratory, managed by Lockheed Martin Energy Research for the US Department of Energy, under contract number DE-AC05-96OR22464. Support for instrumentation came from TA Instruments, and Mettler-Toledo. Research support was also given by ICI Paints.

References

[1] M. Reading, Trends Polym. Sci. 8 (1993) 248.
[2] M. Reading, D. Elliot, V.L. Hill, J. Thermal Anal. 40 (1993) 949.
[3] P.H. Gill, S.R. Sauerbrunn, M. Reading, J. Thermal Anal. 40 (1993) 931.
[4] B. Wunderlich, Y. Jin, A. Boller, Thermochim. Acta 238 (1994) 277.
[5] A. Boller, Y. Jin, B. Wunderlich, J. Thermal Anal. 42 (1994) 307.
[6] Thermochim. Acta 304/305 (1997).
[7] B. Wunderlich, A. Boller, I. Okazaki, K. Ishikiriyama, Thermochim. Acta 304/305 (1997) 125.
[8] A. Boller, C. Schick, B. Wunderlich, Thermochim. Acta 266 (1995) 97.
[9] A. Boller, I. Okazaki, B. Wunderlich, Thermochim. Acta 284 (1996) 1.
[10] I. Okazaki, B. Wunderlich, J. Polym. Sci. B 34 (1996) 2941.
[11] B. Wunderlich, I. Okazaki, J. Thermal Anal. 49 (1997) 57.
[12] I. Okazaki, B. Wunderlich, Macromolecules 30 (1997) 1758.
[13] I. Okazaki, B. Wunderlich, Macromol. Chem. Phys. Rapid Commun. 18 (1997) 313.
[14] B. Wunderlich, Macromolecular Physics, Crystal Melting, vol. 3, Academic Press, New York, 1980.
[15] K. Ishikiriyama, B. Wunderlich, Macromolecules 30 (1997) 4126.
[16] K. Ishikiriyama, B. Wunderlich, J. Polym. Sci. B 35 (1997) 1877.
[17] K. Ishikiriyama, A. Boller, B. Wunderlich, J. Thermal Anal. 50 (1997) 547.
[18] A. Boller, M. Ribeiro, B. Wunderlich, J. Thermal Anal. 54 (1998) 545.
[19] J. Pak, A. Boller, I. Moon, M. Pyda, B. Wunderlich, in: D. Dollimore (Ed.), Proceedings of the 26th NATAS Conference in Cleveland, OH, 26 (1998) 163, submitted for publication in Thermochim. Acta.
[20] W. Chen, A. Toda, B. Wunderlich, in: D. Dollimore (Ed.), Proceedings of the 26th NATAS Conference in Cleveland, OH, 26 (1998) 157, submitted for publication J. Polymer Sci., Part B: Polymer Physics.
[21] W. Chen, B. Wunderlich, in: R.G. Morgan (Ed.), Proceedings of the 25th NATAS Conference in McLean, VA, 7–9 September 1997, p. 637.
[22] W. Chen, M. Dadmun, G. Zhang, A. Boller, B. Wunderlich, Thermochim. Acta. 324 (1998) 87.
[23] B. Wunderlich, Thermal Analysis, Academic Press, Boston, 1990.
[24] D.A. Ditmars, S. Ishihara, S.S. Chang, G. Bernstein, E.D. West, J.S. Res. Natl. Bur. Stand. 87 (1982) 159.
[25] B. Wunderlich, J. Thermal Anal. 48 (1997) 207.
[26] R. Androsch, I. Moon, S. Kreitmeier, B. Wunderlich, Thermochim. Acta (1999), to be published.
[27] M. Jaffe, B. Wunderlich, in: Proceedings of the Second ICTA, in: E.F. Schwenker, P.D. Garn (Eds.), Thermal Analysis, vol. 1, Academic Press, New York, 1969, p. 387.
[28] M. Pyda, A. Boller, J. Grebowicz, H. Chuah, B.V. Lebedev, B. Wunderlich, J. Polym. Sci. Part B: Polymer Phys. 36 (1998) 2499.
[29] R. Androsch, B. Wunderlich, in: D. Dollimore (Ed.), Proceedings of the 26th NATAS Conference in Cleveland, 26 (1998) 460, accepted for publication, Macromolecules.
[30] R. Androsch, Polymer 40 (1998) 2805.

[31] B. Wunderlich, A. Boller, I. Okazaki, S. Kreitmeier, Thermochim. Acta 282/283 (1996) 143.
[32] B. Wunderlich, Pure Appl. Chem. 67 (1995) 1919.
[33] B. Wunderlich, J. Grebowicz, Adv. Polym. Sci 60/61 (1984) 1.
[34] A. Toda, T. Oda, M. Hikosaka, Y. Saruyama, Thermochim. Acta 293 (1997) 47.
[35] A. Toda, T. Oda, M. Hikosaka, Y. Saruyama, Polymer 38 (1997) 47.
[36] A. Toda, C. Tomita, M. Hikosaka, Y. Saruyama, Thermochim. Acta 38 (1997) 2849.
[37] B. Wunderlich, M. Möller, J. Grebowicz, H. Baur, Conformational Motion and Disorder in Low and High Molecular Mass Crystals, Advances in Polymer Science, Springer, Berlin, vol. 87, 1988.
[38] M. Merzlyakow, C. Schick, elsewhere in this issue.
[39] B. Wunderlich, Disc. Faraday Soc. 68 (1979) 239.
[40] B. Wunderlich, Crystallization of polymers, in: M. Dosiére (Ed.), Proceedings of the NATO Advanced Research Workshop on Crystallization of Polymers, Mons, 7–11 September 1992, Kluwer Academic Publishers, Dordrecht.
[41] C. Schick, M. Merzlyakov, B. Wunderlich, Polym. Bull. 40 (1998) 297.
[42] U. Gaur, B. Wunderlich, Macromolecules 13 (1980) 445.
[43] B. Wunderlich, G. Czornyj, Macromolecules 10 (1977) 906.